Обзор ArXiv: astro-ph, 25 мая – 13 июня 2018

От Сильченко О.К.

Astro-ph: 1805.09735

Angular momentum of dwarf galaxies

Sushma Kurapati[1⋆], Jayaram N. Chengalur [1], Simon Pustilnik [2], and Peter Kamphuis
[1] *National Centre for Radio Astrophysics, Tata Institute of Fundamental Research, PO Box 3, Pune 411007, India*
[2] *Special Astrophysical Observatory, Russian Academy of Sciences, Nizhnii Arkhyz, 369167 Russia*

Accepted XXX. Received YYY; in original form ZZZ

ABSTRACT

Mass and specific angular momentum are two fundamental physical parameters of galaxies. We present measurements of the baryonic mass and specific angular momentum of 11 void dwarf galaxies derived from neutral hydrogen (HI) synthesis data. Rotation curves were measured using 3D and 2D tilted ring fitting routines, and the derived curves generally overlap within the error bars, except in the central regions where, as expected, the 3D routines give steeper curves. The specific angular momentum of void dwarfs is found to be high compared to an extrapolation of the trends seen for higher mass bulge-less spirals, but comparable to that of other dwarf irregular galaxies that lie outside of voids. As such, our data show no evidence for a dependence of the specific angular momentum on the large scale environment. Combining our data with the data from the literature, we find a baryonic threshold of $\sim 10^{9.1}$ $M_{\odot}$ for this increase in specific angular momentum. Interestingly, this threshold is very similar

Выборка галактик войдов, наблюдавшихся в HI

Table 1. Parameters of galaxies selected for this study

Name	d (Mpc)	M_B	M_{HI} ($10^7 M_\odot$)	Obs.Date	Telscope
KK246	6.850	-13.69	9.0	09.07.2010	VLA
DDO47	8.040	-14.78	52.3	28.09.1984	VLA
UGC4115	7.730	-14.75	31.9	08.07.2004	VLA
UGC3501	10.07	-13.32	8.6	22.11.2014	GMRT
J0737+4724	10.40	-12.50	1.8	24.11.2011	GMRT
J0926+3343	10.63	-12.90	5.2	21.08.2015	GMRT
UGC5288	11.41	-15.61	90.2	20.01.1999	VLA
UGC4148	13.55	-15.18	78.4	01.10.2015	GMRT
J0630+23	22.92	-15.89	135.1	12.09.2015	GMRT
J0626+24	23.21	-15.64	63.8	03.05.2015	GMRT
J0929+1155	24.29	-14.69	36.6	23.04.2015	GMRT

Notes: All the galaxies except KK246 are from Lynx-Cancer void. All the parameters are taken from Pustilnik & Tepliakova (2011) and from Kreckel et al. (2011a) for the galaxies in Lynx-Cancer void and KK246 respectively.

Удельный момент карликов выше, чем ожидалось по scaling relations спиральных галактик

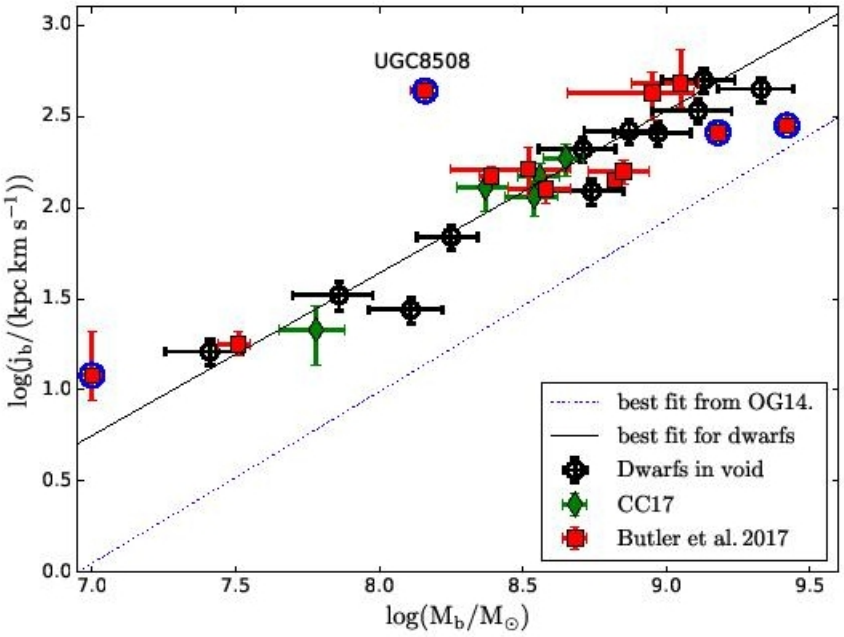

Figure 1. Log j_b-log $M_b$relation of 11 dwarf galaxies residing in Lynx-Cancer void from this work (black open circles), 12 dwarf galaxies from Butler et al. (2017) (red squares) and 5 dwarf galaxies from Chowdhury & Chengalur (2017) (green diamonds). The blue dotted line indicates the $\beta = 0$ plane of j_b- $M_b$relation obtained for the massive spiral galaxies by Obreschkow & Glazebrook (2014) and was recomputed by Chowdhury & Chengalur (2017). The black solid line is the best fit line for the dwarf galaxies using the linear regression. The galaxies from Butler et al. (2017) that were identified as being discrepant are marked with a circle around the red squares.

Т.к. окружение не сыграло, объединили выборки войдов и Butler

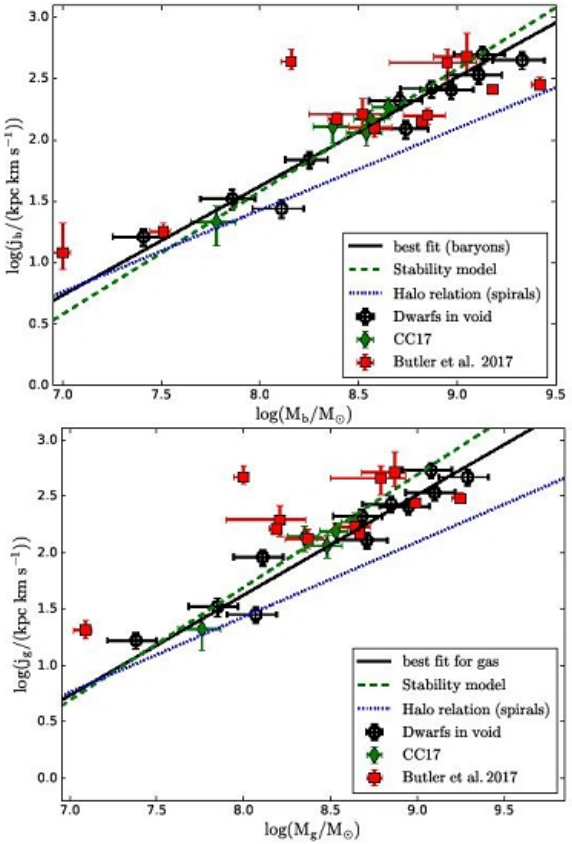

Figure 2. (a). The Log j_b- Log $M_b$plane and (b) Log j_{gas}- Log M_{gas} plane showing data for 11 dwarf galaxies residing in Lynx-Cancer void (black open circles) as well as dwarf galaxies for which we have taken the data from the literature. The black solid line indicates the best fit linear relation to the entire sample. The green dotted line is the best-fit stability model (Eqn 6) for a rising rotation curve. The best fit stability model corresponds to $\sigma/Q_c \sim 2.8$ km s^{-1}and ~ 2.2 km s^{-1}for the fit to the baryons and the gas respectively. The dotted line is from Obreschkow & Glazebrook (2014) and shows the $j \propto M^{2/3}$ relation expected from the tidal torquing model. See the text for more details.

- Вообще говоря, зависимость больше похожа на прямо-пропорциональную, а это предсказывал Засов (и Наташа Зайцева)! (маржинальная грав. устойчивость). Пибблз отдыхает.

Astro-ph: 1805.12132

WHY POST-STARBURST GALAXIES ARE NOW QUIESCENT

K. Decker French[†]
Observatories of the Carnegie Institute for Science, 813 Santa Barbara Street, Pasadena CA 91101
Steward Observatory, University of Arizona, 933 North Cherry Avenue, Tucson AZ 85721

Ann I. Zabludoff
Steward Observatory, University of Arizona, 933 North Cherry Avenue, Tucson AZ 85721

Ilsang Yoon
National Radio Astronomy Observatory, 520 Edgemont Road, Charlottesville, VA 22903

Yancy Shirley
Steward Observatory, University of Arizona, 933 North Cherry Avenue, Tucson AZ 85721

Yujin Yang
Korea Astronomy and Space Science Institute, 776 Daedeokdae-ro, Yuseong-gu, Daejeon 305-348, Korea
Korea University of Science and Technology (UST), 217 Gajeong-ro Yuseong-gu, Daejeon 34113, Korea

Adam Smercina
Department of Astronomy, University of Michigan, 1085 S. University Avenue, Ann Arbor, MI 48109

J.D. Smith
Department of Physics and Astronomy, University of Toledo, Ritter Obs., MS #113, Toledo, OH 43606

Desika Narayanan
Department of Astronomy, University of Florida, 211 Bryant Space Sciences Center, Gainesville, FL 32611
n Center (DAWN), Niels Bohr Institute, University of Copenhagen, Juliane Maries vej 30, DK-2100 Copenhagen,

Собственно, всего лишь искали плотный газ в двух poststarbursts

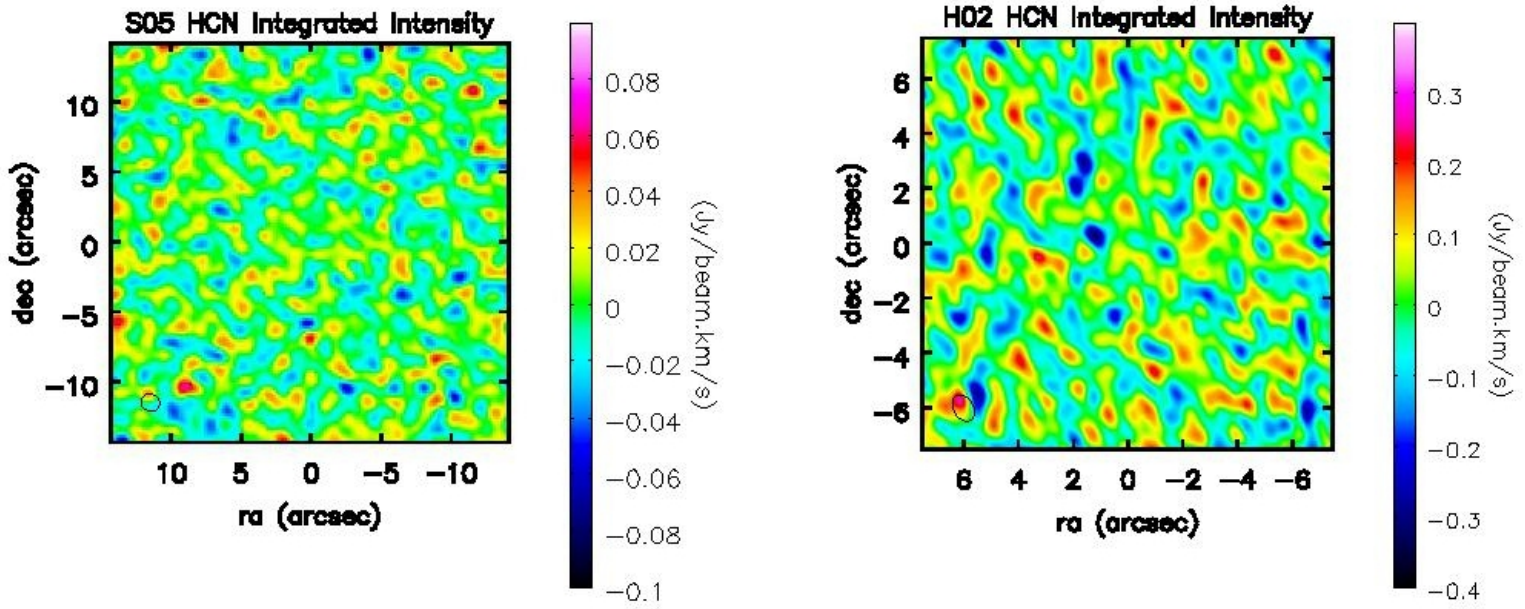

Figure 1. Integrated intensity maps for the two post-starburst targets for HCN (1–0). The galaxy optical centers are at (0,0) on each plot. Neither source is detected.

- не нашли!

То есть SF прекращается НЕ потому, что кончается газ; а потому, что он перестает переходить в плотную фазу

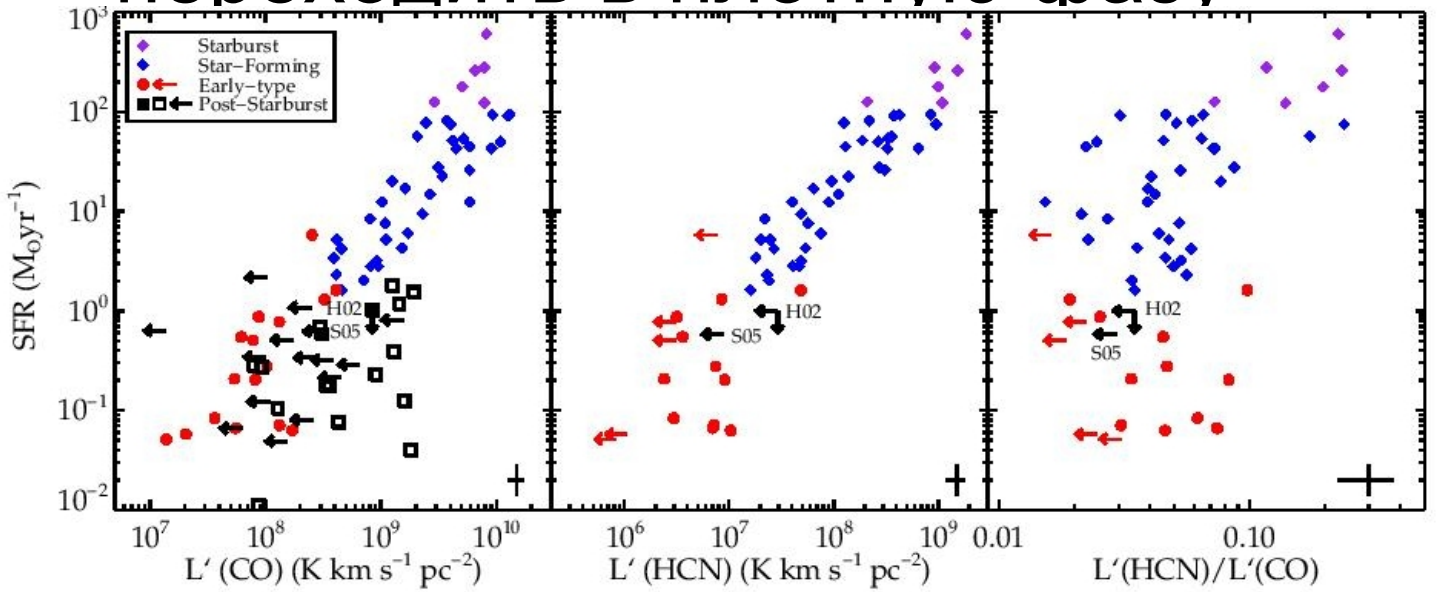

Figure 2. **Left:** SFR vs. L'(CO) for star-forming and starbursting galaxies from Gao & Solomon (2004) (blue and purple diamonds), early type galaxies from Crocker et al. (2012) (red circles and arrows), and post-starburst galaxies French et al. (2015) (black squares and arrows). Filled black squares represent the two galaxies targeted for dense gas observations. Characteristic error bars are shown in the bottom right of each panel. All upper limits are at the 3σ level. The post-starburst galaxies have systematically low SFRs for their CO luminosities. The two post-starburst galaxies targeted for HCN observations are representative of the post-starburst population. **Middle:** SFR vs. L'(HCN) for the same samples. HCN is not detected for either post-starburst galaxy studied here, consistent with their low SFRs and with the early type galaxies. The absence of denser gas traced by HCN reveals why the SFRs of post-starburst galaxies are so low. **Right:** SFR vs. dense gas luminosity ratio L'(HCN)/L'(CO). The post-starburst galaxies targeted here have low HCN/CO luminosity ratios compared with the starbursting, star-forming and many CO-detected early type galaxies. The low HCN/CO luminosity ratios of the post-starbursts indicate the dense molecular gas fraction has changed since the starbursting phase and is different than in normal star-forming galaxies.

Astro-ph: 1806.02886

Morphology and kinematics of orbital components in CALIFA galaxies across the Hubble sequence

Ling Zhu[1⋆] , Glenn van de Ven[2,1], Jairo Méndez-Abreu[3,4], Aura Obreja[5].
[1] *Max Planck Institute for Astronomy, Königstuhl 17, 69117 Heidelberg, Germany*
[2] *European Southern Observatory, Karl-Schwarzschild-Str. 2, 85748 Garching b. München, Germany*
[3] *Instituto de Astrofisica de Canarias C/ Via Lactea, s/n, E-38205, La Laguna, Tenerife, Spain*
[4] *Departamento de Astrofísica, Universidad de La Laguna, E-38200 La Laguna, Tenerife, Spain*
[5] *University Observatory Munich, Scheinerstr. 1, D-81679 Munich, Germany*

ABSTRACT
Based on the stellar orbit distribution derived from orbit-superposition Schwarzschild models, we decompose each of 250 representative present-day galaxies into four orbital components: cold with strong rotation, warm with weak rotation, hot with dominant random motion and counter-rotating (CR). We rebuild the surface brightness (Σ) of each orbital component and we present in figures and tables a quantification of their morphologies using the Sersic index n, concentration $C = \log(\Sigma_{0.1R_e}/\Sigma_{R_e})$ and intrinsic flattening $q_{\rm Re}$ and $q_{\rm Rmax}$, with R_e the half-light-radius and $R_{\rm max}$ the CALIFA data coverage. We find that: (1) kinematic hotter components are generally more concentrated and rounder than colder components, and (2) all components become more concentrated and thicker/rounder in more massive galaxies; they change from

Подход к динамическому анализу

We created orbit-superposition Schwarzschild models (van den Bosch et al. 2008) which simultaneously fit the observed surface brightness and stellar kinematics for each galaxy (Zhu et al. 2018b). Orbits are characterized by two main properties: the time-averaged radius r representing the size of each orbit, and circularity, $\lambda_z \equiv J_z/J_{\rm max}(E)$ around the short z axis, normalised by the maximum of a circular orbit with the same binding energy E. Circular orbits

2.2 Orbital decomposition

The technique of orbital decomposition has been described in detail in Zhu et al. (2018b). Given the overall circularity distribution, $p(\lambda_z)$, we divide the orbits within $1\,R_e$ into four components: cold ($0.8 \leq \lambda_z \leq 1$), warm ($0.25 < \lambda_z < 0.8$), hot ($-0.25 \leq \lambda_z \leq 0.25$) and counter-rotating (CR; $\lambda_z < -0.25$). We denote the galaxy's stellar orbit distribution within $1\,R_e$ as luminosity fractions of four components: $f_{\rm cold}$, $f_{\rm warm}$, $f_{\rm hot}$, and $f_{\rm CR}$. The separation and orbit fractions are the same as in Zhu et al. (2018a). The uncertainties

Выборка из 260 галактик разных морфологических типов и масс

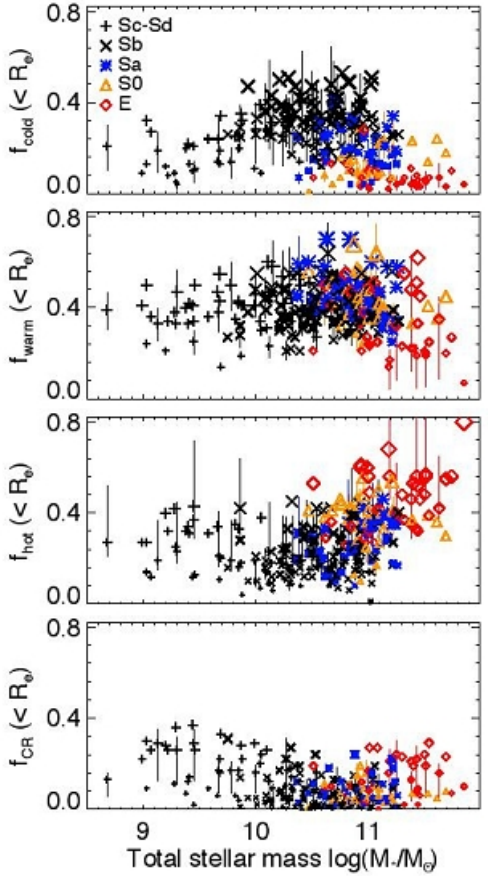

Figure 1. Orbit fractions as function of galaxy's total stellar mass M_*. From top to bottom; cold, warm, hot and CR orbital fractions ($f_{\rm cold}, f_{\rm warm}, f_{\rm hot}, f_{\rm CR}$). Black pluses, black crosses, blue asterisks, orange triangles and red diamonds represent Sc-Sd, Sb, Sa, S0 and E galaxies, with symbol sizes indicating the luminosity fractions. The short vertical lines indicate the $1\,\sigma$ uncertainties, including both statistical uncertainties as well as systematic biases and uncertainties as inferred from tests with simulated galaxies (Zhu et al. 2018a), we have errors for all, but only shown that

Пять типичных примеров с ребра

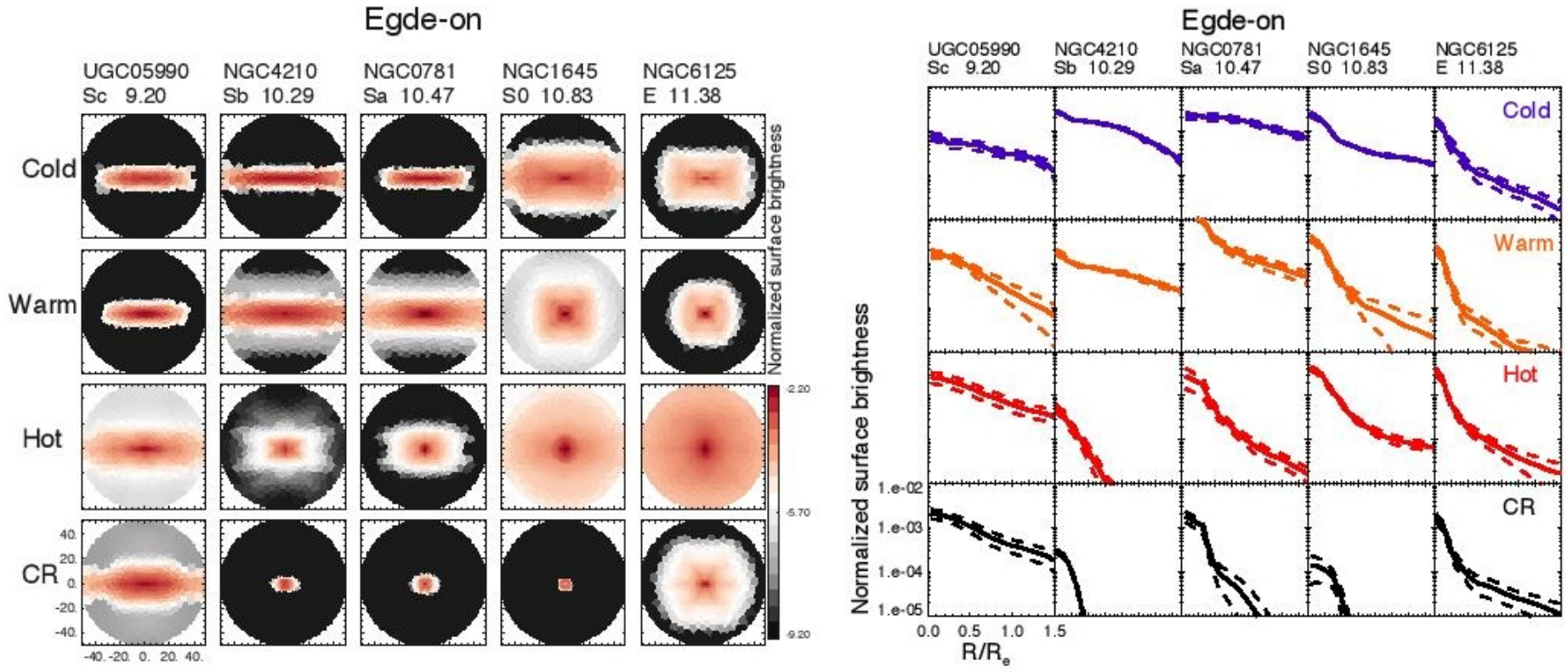

Figure 2. The edge-on projected surface brightness of the cold, warm, hot, and CR components for five representative galaxies. The name of the galaxies are listed at the top of columns, as well as their Hubble types and their total stellar masses as $\log(M_*/M_\odot)$. In the left panels, we show the 2D surface brightness of the best-fitting model. The colorbars indicate the values of the normalized surface brightness in $\log(L/\mathrm{arcsec}^2)$, with the same scale for all panels, the total luminosity within $1\,R_e$ of each galaxy is normalized to unity. All panels share the same x and y axis range from -50 to 50 arcsec, as shown in the bottom-left panels. In the right panels, we show the mean (solid line) and $1\,\sigma$ scatter (dashed lines) of the 1D SB along major axis from the models within $1\,\sigma$ confidence level, with x axis in R/R_e, y axis in the same unit as the density maps on the left.

И вот как-то слабо связана динамика с морфологией…

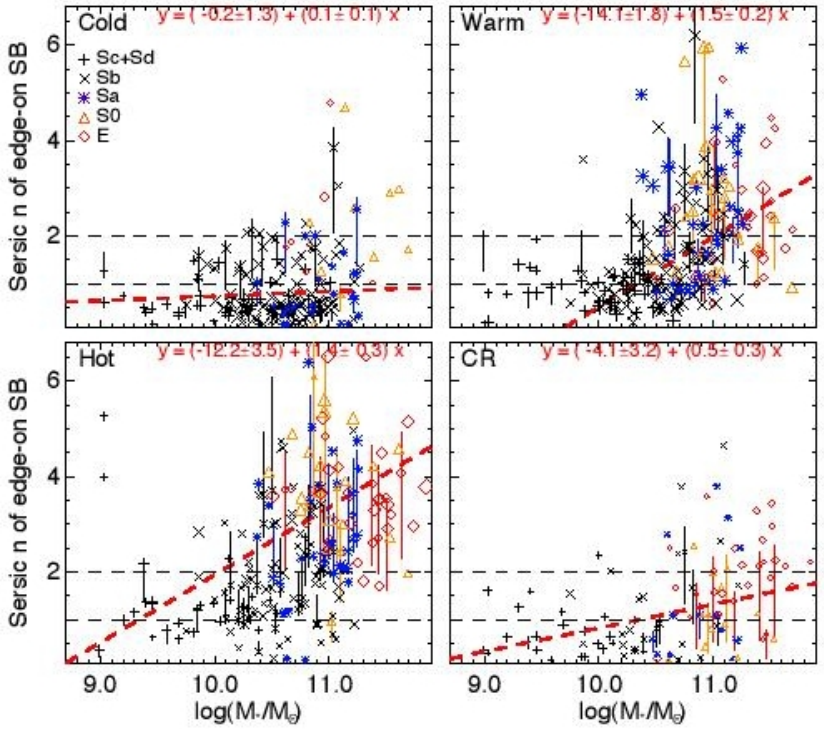

Figure 4. The resulting Sersic index n of cold, warm, hot, and CR components as a function of galaxy's total stellar mass M_*. Black pluses, black crosses, blue asterisks, yellow triangles, and red diamonds represent Sc/Sd, Sb, Sa, S0, and E galaxies, respectively, with symbol size indicating the orbital fraction. We only obtain a reasonable fit when one component has a relative large luminosity fraction $\gtrsim 0.1$. As a result, there are 164, 230, 207, and 102 points shown in the panels of cold, warm, hot and CR components, respectively. The short vertical lines indicate the 1σ uncertainties of the points including the systematic bias and

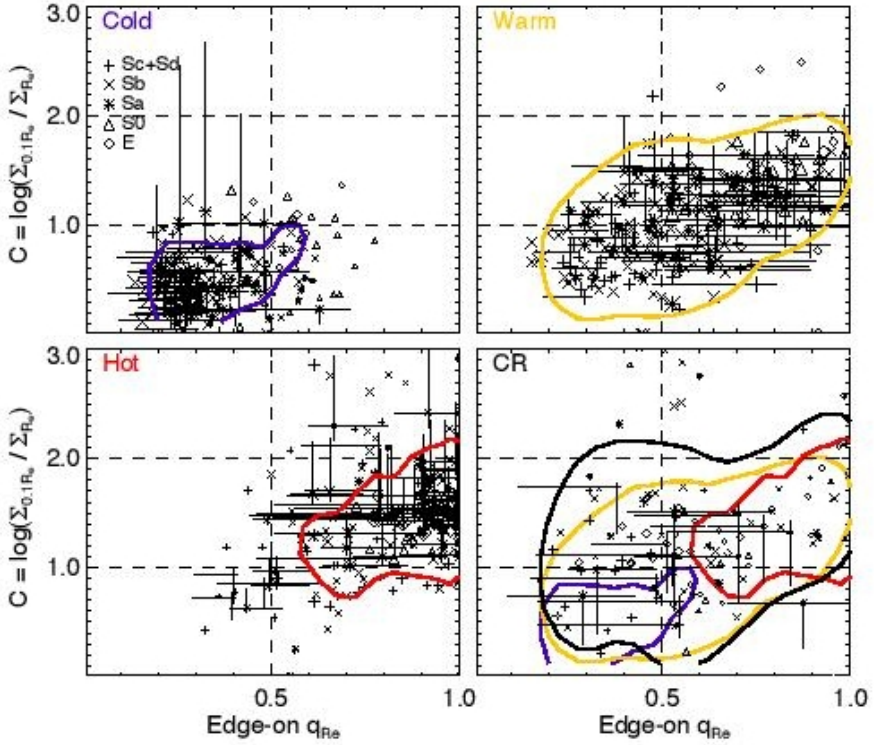

Figure 9. Concentration C vs. the intrinsic flattening $q_{\rm Re}$. The short horizontal and short vertical lines indicate the $1\,\sigma$ uncertainties of $q_{\rm Re}$ and C, including the systematic bias and systematic errors as shown in the Appendix A, we have errors for all, but only shown for randomly 1/5 of the points. The blue, yellow, red and black contours enclose $\sim 80\%$ of the points for cold, warm, hot and CR components in the diagram. The vertical dashed represents $q_{\rm Re} = 0.5$, while the two horizontal dashed lines are $C = 1$ and $C = 2$, respectively. In the CR panel, we overplot the contours of all four components for comparison. In general, one component is more concentrated when it is rounder. The cold and hot components are well separated on this diagram, while the warm component overlaps with the cold and hot components at both

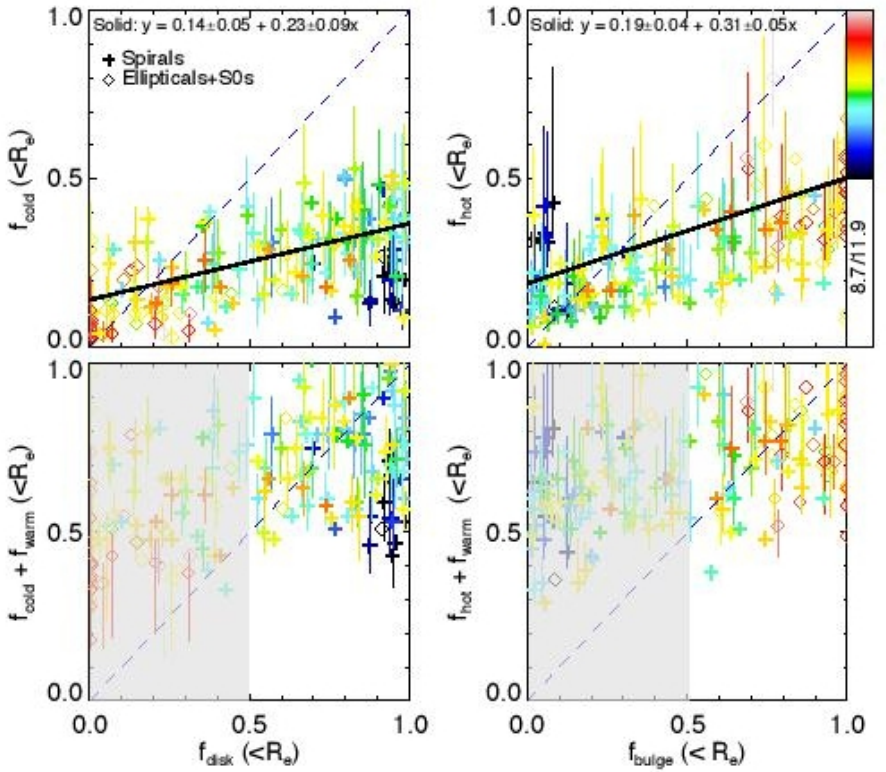

Figure 10. Orbital fractions compared with the photometric bulge/disk fraction; $f_{\rm cold}$ vs. $f_{\rm disk}$ (top-left), $f_{\rm hot}$ vs. $f_{\rm bulge}$ (top-right), $f_{\rm cold} + f_{\rm warm}$ vs. $f_{\rm disk}$ (bottom-left), and $f_{\rm hot} + f_{\rm warm}$ vs. $f_{\rm bulge}$ (bottom-right). Each plus represents a late-type galaxy and a diamond represents an early-type galaxy, colored with their stellar masses in $\log 10(M_*/M_\odot)$ as indicated by the color bar. The short vertical lines indicate the $1\,\sigma$ uncertainties, including the systematic bias and systematic errors as described in Section 2, we have errors for all, but only shown that for randomly 1/2 of the points. The blue dashed line represents $y = x$, the solid black line illustrates the best linear fits as indicated by the equations. The very low-mass galaxies with $M_* < 10^{10}\,M_\odot$ (dark blue points) are outliers of these relations. In low mass late-type galaxies, gold

Псевдобалджи?

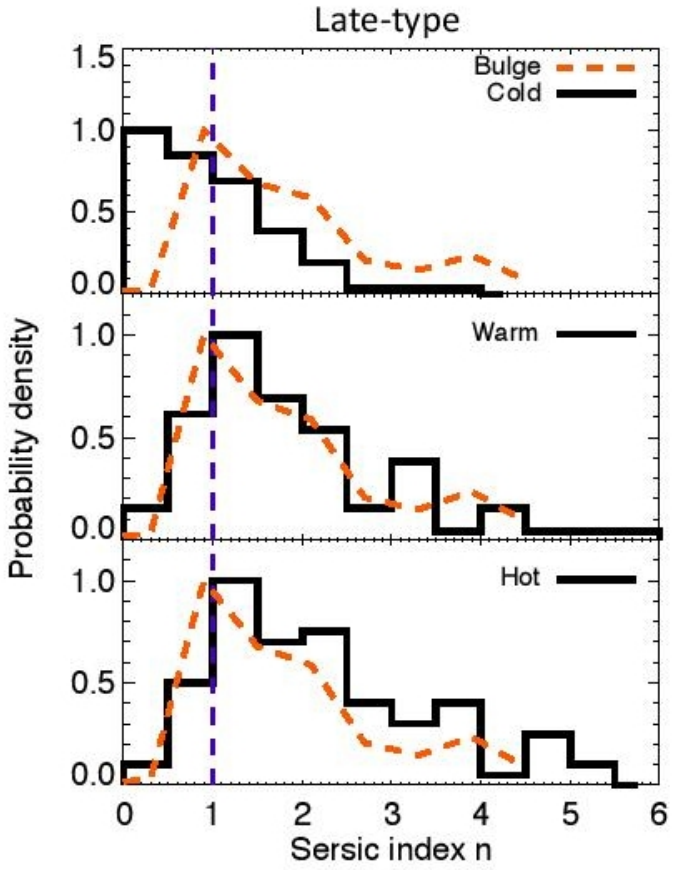

Figure 11. Sersic index n of the orbital components compared with those of the photometric bulges, for late-type galaxies only. The orange dashed curve is n of bulges from Méndez-Abreu et al. (2017), the black histogram are n distribution of cold, warm, and hot components from top to bottom. The vertical dashed line is $n = 1$, which is fixed for an exponential disk.

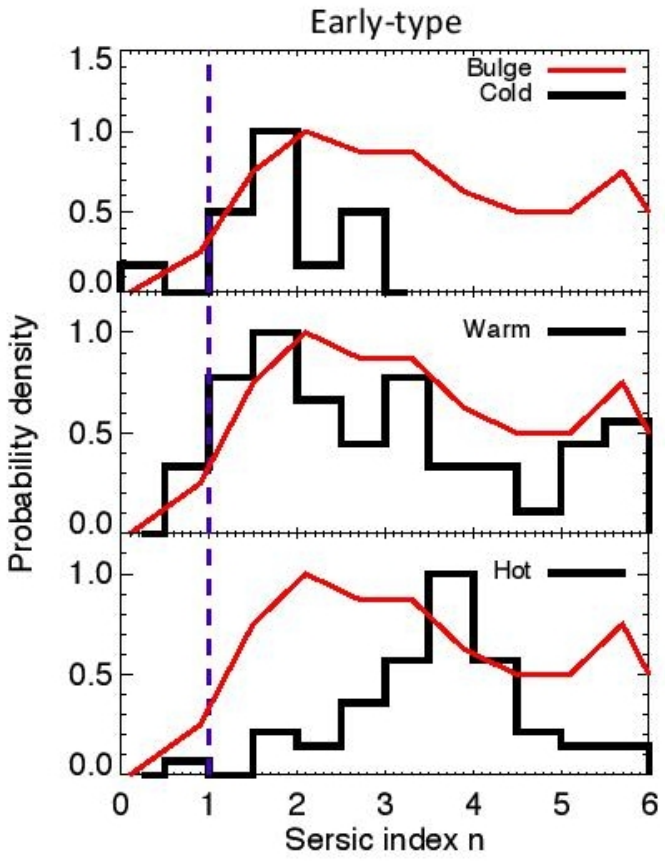

Figure 12. Sersic index n of the orbital components compared with those of the photometric bulges, but for early-type galaxies. The red solid curve is n of bulges from Méndez-Abreu et al. (2017), the black histogram are n distribution of cold, warm, and hot components from top to bottom. The vertical dashed line is $n = 1$, which is fixed for an exponential disk.

Astro-ph: 1806.03311

Widespread star formation inside galactic outflows

R. Gallagher,[1,2] R. Maiolino,[1,2] F. Belfiore,[3] N. Drory,[4] R. Riffel,[5,6] R.A. Riffel,[6,7]
[1]*Cavendish Laboratory, University of Cambridge, 19 J. J. Thomson Ave., Cambridge CB3 0HE, UK*
[2]*Kavli Institute for Cosmology, University of Cambridge, Madingley Road, Cambridge CB3 0HA, UK*
[3]*University of California Observatories - Lick Observatory, University of California Santa Cruz, 1156 High St., Santa Cruz, CA 95064, USA*
[4]*McDonald Observatory, The University of Texas at Austin, 2515 Speedway Stop C1402, Austin, TX 78712, USA*
[5]*Departamento de Astronomia, Av. Bento Goncalves 9500, Agronomia, Porto Alegre, RS, Brazil*
[6]*Laboratório Interinstitucional de e-Astronomia, Rua General José Cristino, 77 Vasco da Gama, Rio de Janeiro, Brazil, 20921-400*
[7]*Departamento de Fisica, Universidade Federal de Santa Maria, CEP 97105-900 Santa Maria, RS - Brazil*

Accepted . Received

ABSTRACT
Several models have predicted that stars could form inside galactic outflows and that this would be a new major mode of galaxy evolution. Observations of galactic outflows have revealed that they host large amounts of dense and clumpy molecular gas, which provide conditions suitable for star formation. We have investigated the properties of the outflows in a large sample of galaxies by exploiting the integral field spectroscopic data of the large MaNGA-SDSS4 galaxy survey. We find that star formation occurs inside at least half of the galactic outflows in our sample. We also show that even if star formation is prominent inside

И откуда же берутся данные по истечениям?...

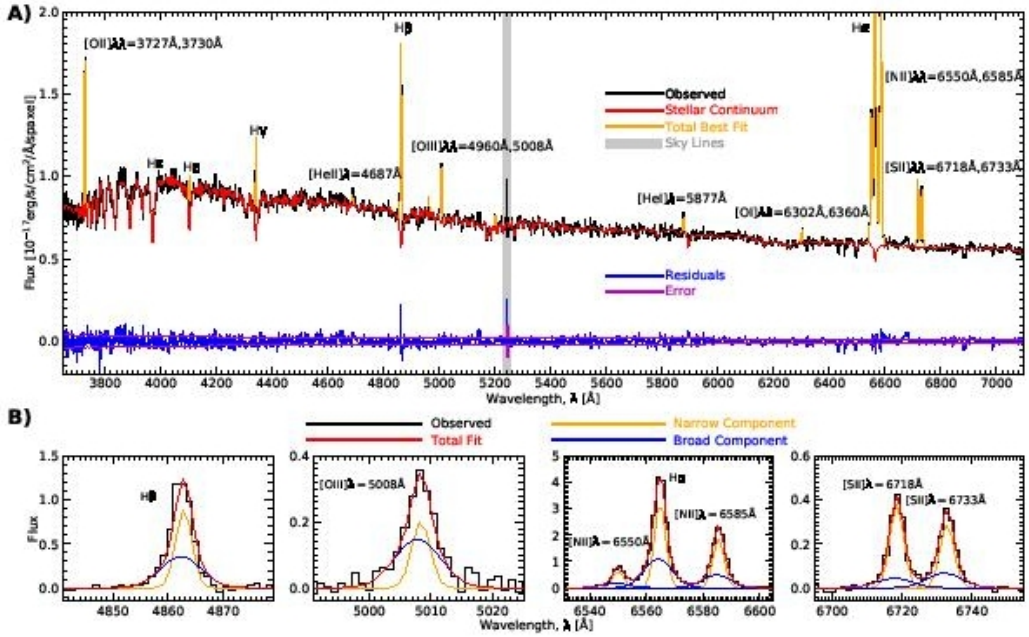

Figure 1. Example of simultaneous stellar continuum and emission line fit to the spectrum extracted from the central region of a representative galaxy in our sample. A: Full spectrum decomposition showing the simultaneous stellar continuum (red) and emission line (orange) fit to spectrum. Shown below the fit are the residuals (blue) and the error spectrum (magenta) for the galaxy. The OII 5577 sky line has been masked, shown here by the grey shaded area. B: Subsections of continuum-subtracted spectra, showing some of the relevant emission lines used in the analyses. The decomposition of the narrow (orange) and broad (blue) components can be seen, alongside the total fit of the two components (red).

… из BPT-диагностики широких компонент эмиссионных линий. SF!

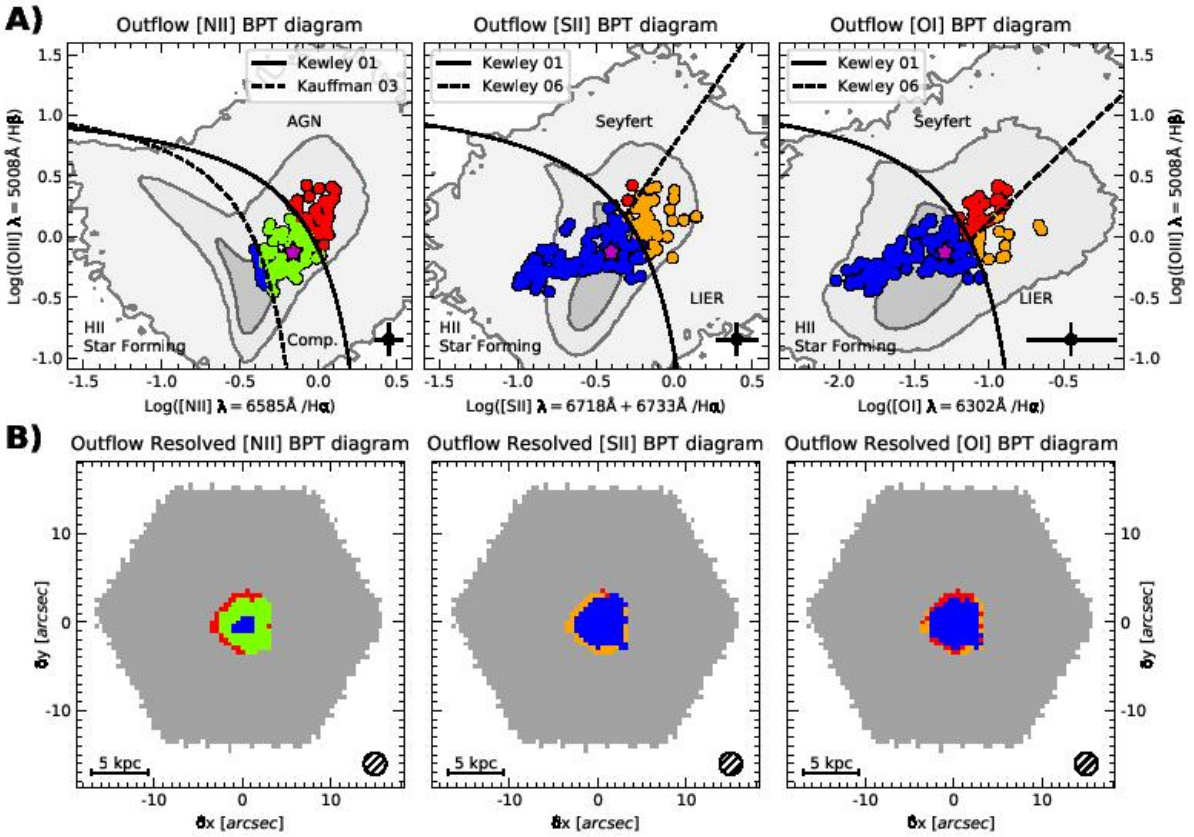

Figure 4. A: Distribution of the broad (outflow) component of the nebular lines on the BPT diagrams for the same representative galaxy of Fig.1 and Fig.2. A significant fraction of this galactic outflow is in the BPT regions typically populated by star forming regions and star forming galaxies. The magenta star shows the median location of the BPT points in the outflow. The background grey-scale contours indicate the distribution of several hundred thousand galaxies n the SDSS survey. B: Spatially resolved BPT classification of the outflowing gas, using the same colour coding as in (A). The central region of the outflow

Статистика

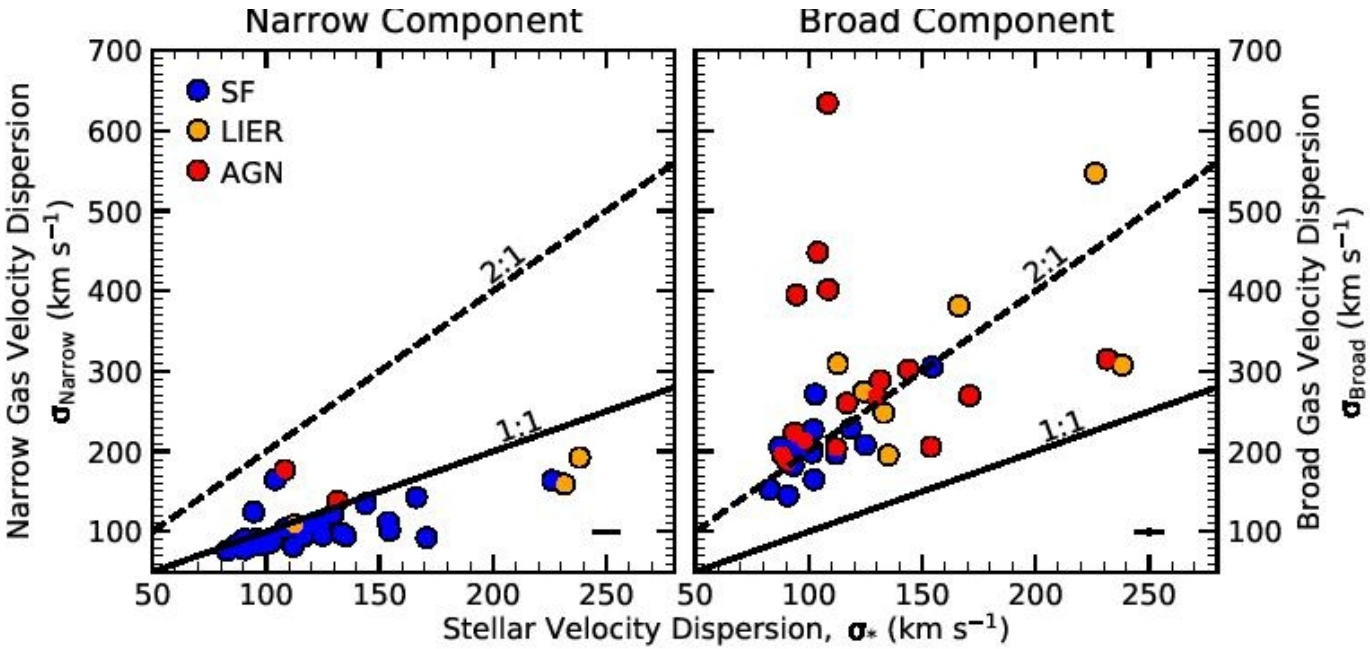

Figure 3. Left: Velocity dispersion of the narrow component of the nebular lines in the central region compared with the stellar velocity dispersion. As expected, the narrow component has a velocity dispersion similar to the stellar velocity dispersion, or even lower, owing to the fact that the gas disc is generally dynamically colder than stars. Right: Velocity dispersion of the broad component of the nebular lines in the central region compared with the stellar velocity dispersion in the same region. The former is much larger than the latter, indicating that the broad component cannot result from beam smearing effects of the central rotation curve and that it must be associated with non-virial motions, i.e. outflows.

Статистика по звездообразованию в истечениях

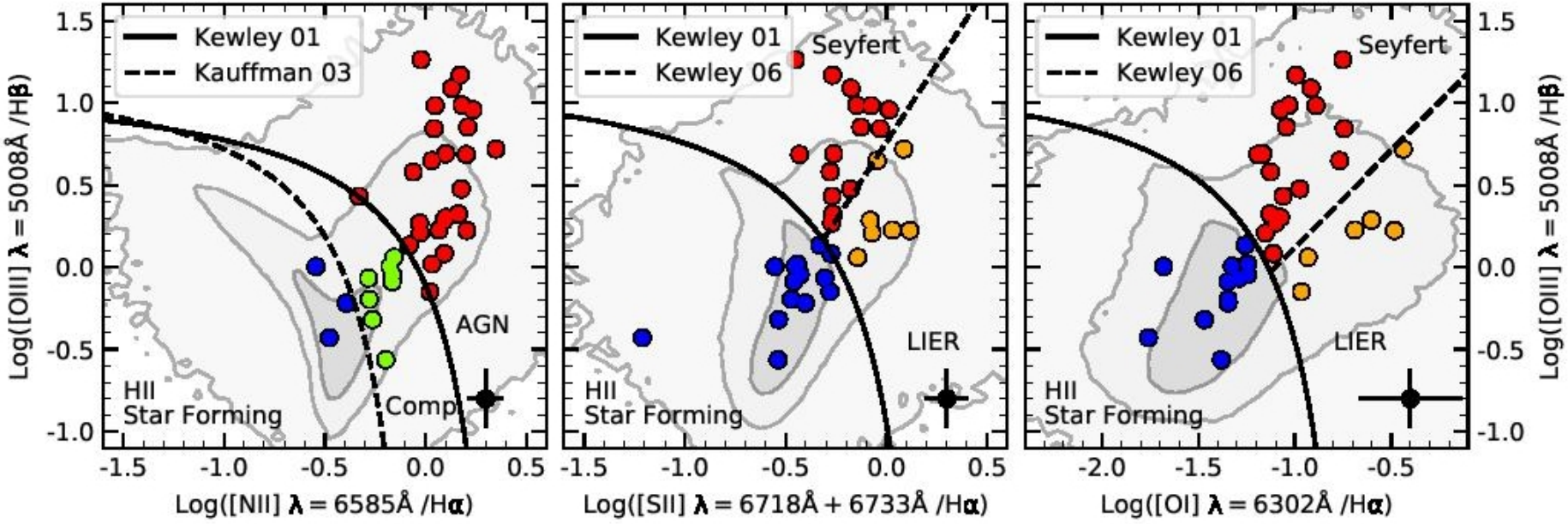

Figure 5. Median BPT classification of the outflows for the galaxies in our sample. According to their median BPT classification in the [SII] and [OI] diagrams (central and right panes), about 30% of the galactic outflows in our sample are "star forming". The same applies to the [NII] classification if one includes galaxies classified as "composite" (however, one should take into account that the [NII] classification is more ambiguous, as discussed in the text).

Треть всего SF – внутри ветра

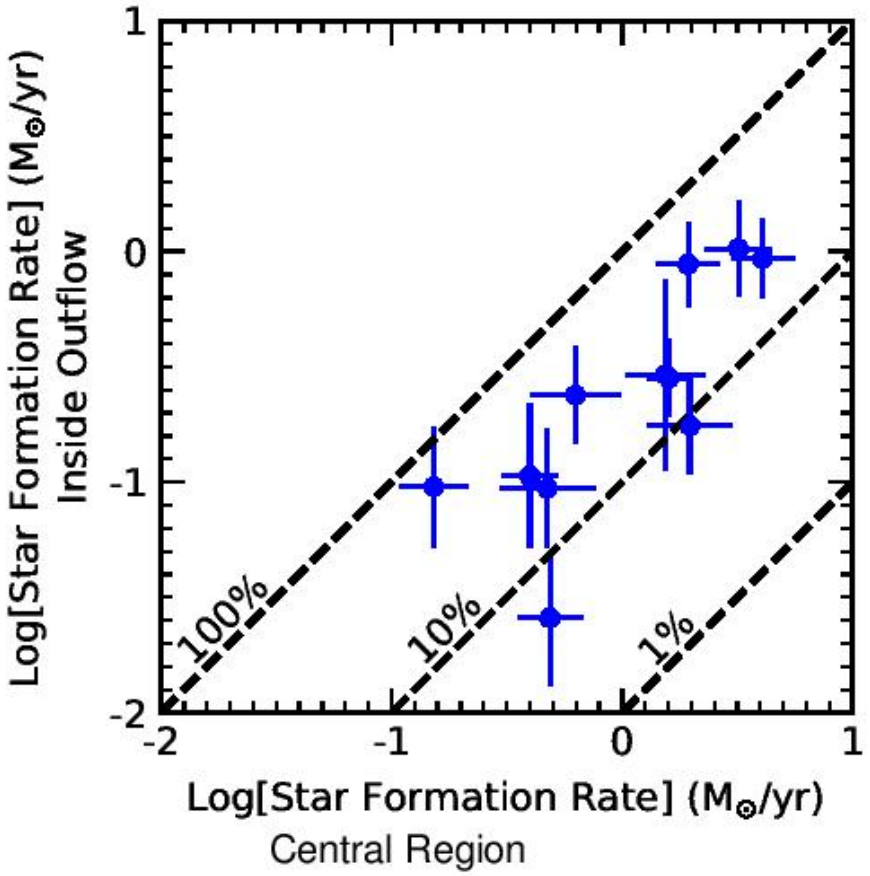

Figure 9. Star formation rate inside the outflow as a function of the star formation rate in the same central projected area in which the outflow is detected.

Это массивные спиральные галактики главной последовательности

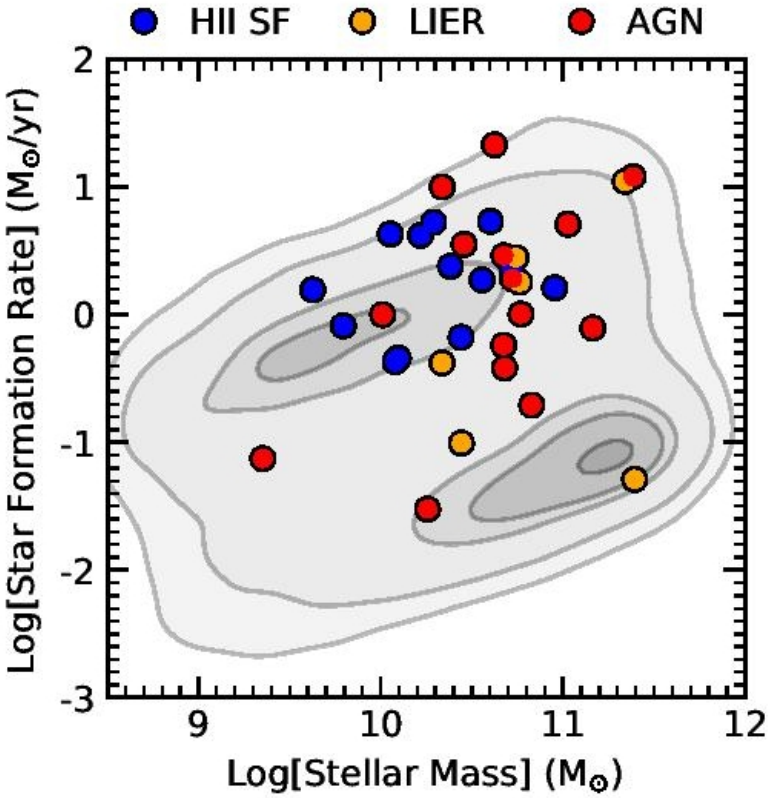

Figure 12. Star formation rate versus stellar mass diagram. The background contour plot shows the distribution of all 2,800 galaxies in the MaNGA sample. The symbols show the distribution of galaxies with outflows presented in this study, i.e. those for which the outflows can be analysed in the BPT diagram. The BPT classification of the outflow is the same as in the [SII]-BPT diagram of Fig.5. Most outflows, especially those hosting star formation inside the outflow, are located around the massive end of the Main Sequence, or slightly above it.

Astro-ph: 1806.04142

EVIDENCE OF ENVIRONMENTAL QUENCHING AT REDSHIFT $Z \approx 2$

ZHIYUAN JI[1], MAURO GIAVALISCO[1], CHRISTINA C. WILLIAMS[2], SANDRA M. FABER[3], HENRY C. FERGUSON[4], YICHENG GUO[3,7], TENG LIU [1,6], BOMEE LEE [1,5]

[1]University of Massachusetts Amherst, 710 North Pleasant St, Amherst, MA 01003-9305, USA, zhiyuanji@astro.umass.edu

[2]Steward Observatory, 933 N. Cherry Ave., University of Arizona, Tucson, AZ 85721, USA

[3]University of California Observatories/Lick Observatory, University of California, Santa Cruz, CA 95064, USA

[4]Space Telescope Science Institute, 3700 San Martin Boulevard, Baltimore, MD, 21218, USA

[5]Infrared Processing and Analysis Center, California Institute of Technology, Pasadena, CA 91125, USA

[6]University of Science and Technology of China, Hefei, Anhui, 230026, China

[7]Department of Physics and Astronomy, University of Missouri, Columbia, MO, 65211, USA

ABSTRACT

We report evidence of "environmental quenching" among galaxies at redshift ≈ 2, namely the probability that a galaxy quenches its star formation activity is enhanced in the regions of space in proximity of other quenched, more massive galaxies. The effect is observed as strong clustering of quiescent galaxies around quiescent galaxies on angular scales $\theta \leq 20$ arcsec, corresponding to a proper(comoving) scale of 168 (502) kpc at $z = 2$. The effect is observed only for quiescent galaxies around other quiescent galaxies; the probability to find star-forming galaxies around quiescent or around star-forming ones is consistent with the clustering strength of galaxies of the same mass and at the same redshift, as observed in dedicated studies of galaxy clustering. The effect is mass dependent in the sense that the quenching probability is stronger for galaxies of smaller mass ($M_* < 10^{10} M_\odot$) than for more massive ones, i.e., it follows the opposite trend with mass relative to gravitational galaxy clustering. The

Галактики без SF на z=2 (GOODS) скучены сильнее, чем любые другие

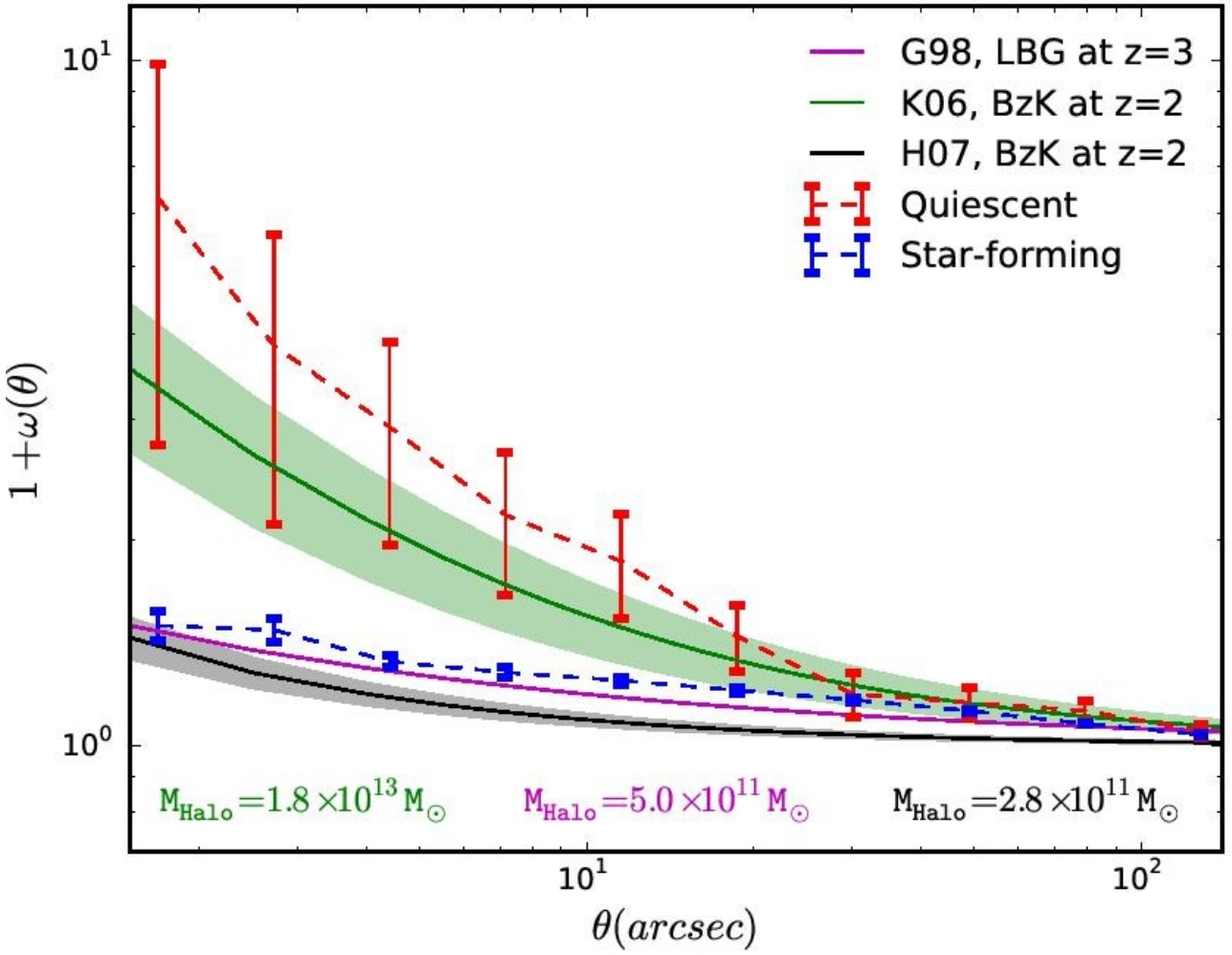

… и это НЕ эффект массы

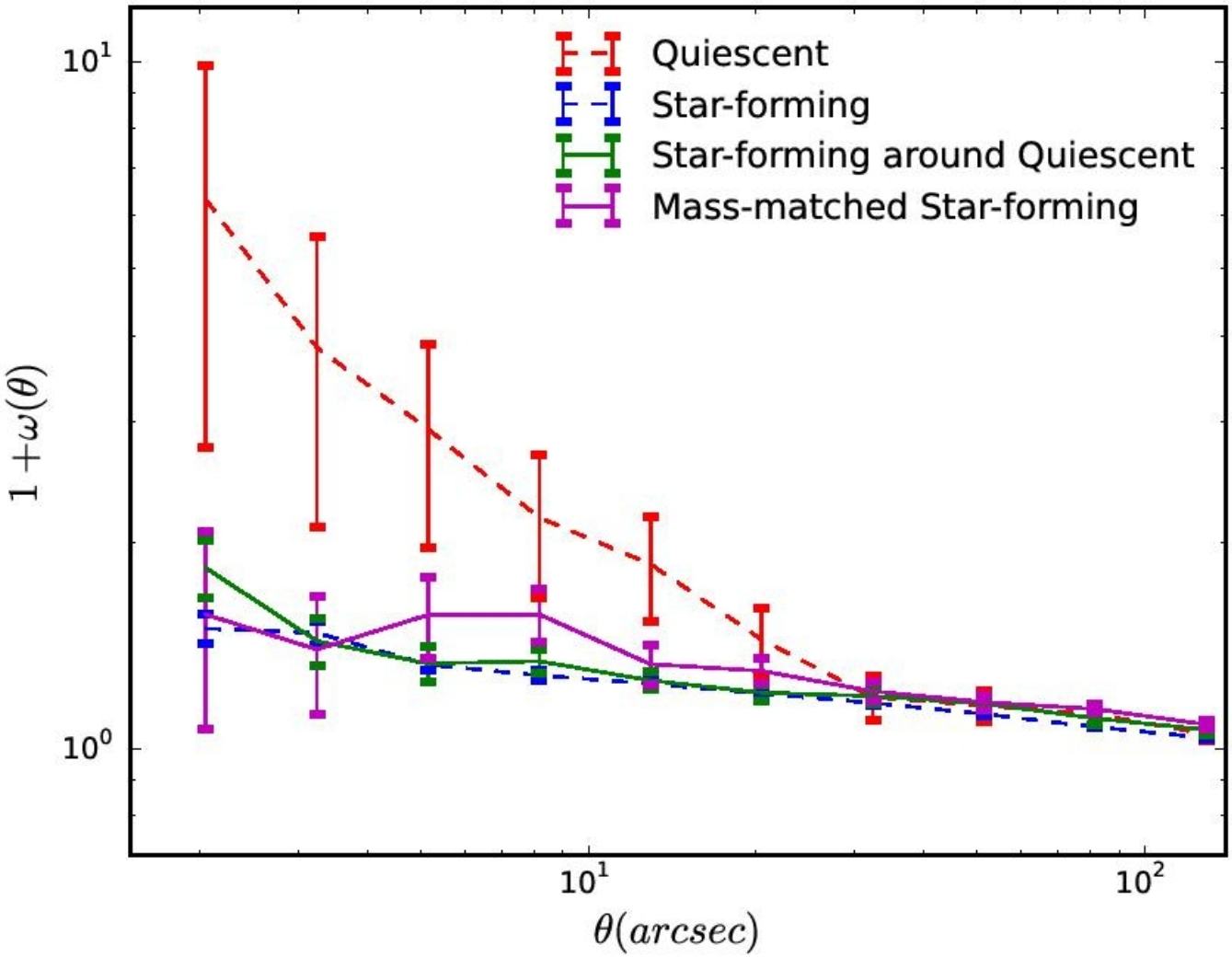

Хотя чем массивнее галактика, тем раньше она заканчивает SF

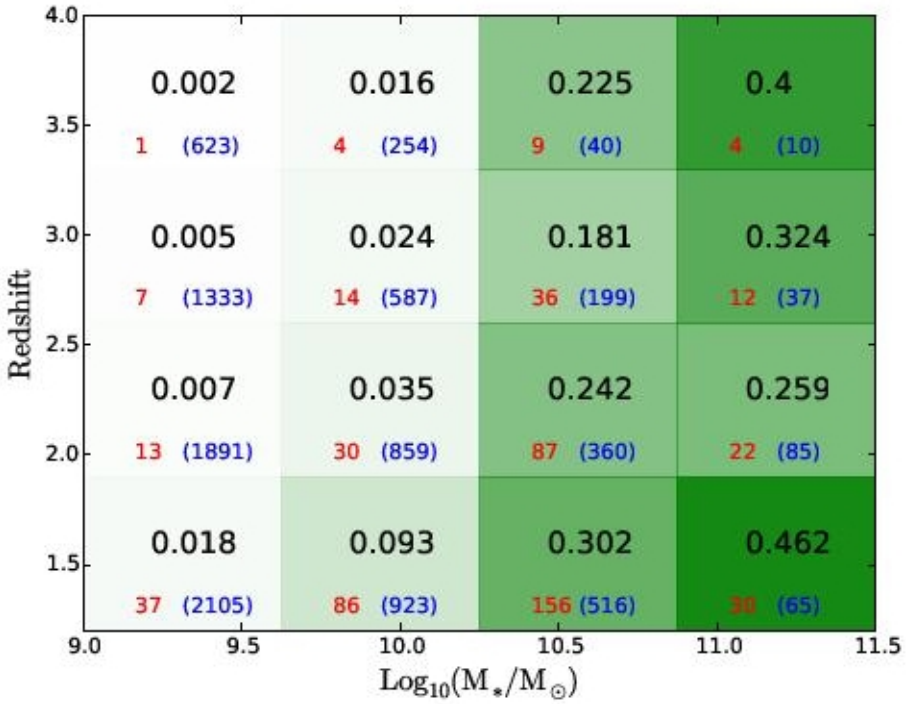

Figure 9. Quenched fraction as a function of stellar mass and redshift. In each bin, the number in black is the quenched fraction, the number in red is the number of quiescent galaxies and the number in blue is the total number of galaxies.